JOURNAL OF SPACECRAFT AND ROCKETS
Vol. 44, No. 5, September–October 2007

Numerical Investigation of Transitional Supersonic Base Flows with Flow Control

Jayahar Sivasubramanian,[*] Richard D. Sandberg,[†] Dominic A. von Terzi,[‡] and Hermann F. Fasel[§]
University of Arizona, Tucson, Arizona 85721

DOI: 10.2514/1.28673

Drag reduction by means of flow control is investigated for supersonic base flows at $M = 2.46$ using direct numerical simulations and the flow simulation methodology. The objective of the present work is to understand the evolution of coherent structures in the flow and how flow control techniques can modify these structures. For such investigations, simulation methods that capture the dynamics of the large turbulent structures are required. Direct numerical simulations are performed for transitional base flows at $Re_D = 30,000$. Because of the drastically increased computational cost of direct numerical simulations at higher Reynolds numbers, a hybrid methodology (flow simulation methodology) is applied to simulate base flows with flow control at $Re_D = 100,000$. Active and passive flow control techniques that alter the near wake by introducing axisymmetric and longitudinal perturbations are investigated. A detailed analysis of the dynamics of the resulting turbulent structures is presented.

Nomenclature

A_{dist} = disturbance amplitude
c_p = pressure coefficient
c_T = coefficient for turbulent time scale
c_v = specific heat
E = total energy $E = c_v T + \frac{1}{2} u_i u_i$
$f_{\varepsilon 2}$ = wall-damping function
$f(\Delta / L_k)$ = contribution function
H = resolved total enthalpy
K = turbulent kinetic energy
k = azimuthal Fourier mode number
L_k = Kolmogorov length scale
M, M_T = Mach number, turbulent Mach number
Pr, Pr_T = Prandtl number, turbulent Prandtl number
p = pressure
Q = second invariant of the velocity gradient tensor
Q_k = turbulent heat flux
q_k = heat-flux vector
Re = Reynolds number
S_{ij} = strain-rate tensor
T = temperature
u_i = velocity vector
W_{ik} = vorticity tensor
z, r, θ = streamwise, radial, and azimuthal coordinates
γ = ratio of specific heats
Δ = computational grid size
δ_{ik} = Kronecker operator
ε = turbulent dissipation rate
μ = dynamic viscosity
μ_T = turbulent eddy viscosity
Π = source term
ρ = density
σ_{ij} = subgrid stress tensor
$\underline{\tau}_{ik}$ = stress tensor
$\underline{\phi}$ = Reynolds average of ϕ
$\tilde{\phi}$ = Favre average of ϕ

Subscripts

D = quantity based on the diameter of the cylinder
i, j, k = indices for the Cartesian tensor notation
K = transport equation for the turbulent kinetic energy
T = turbulent
ε = transport equation for the turbulent dissipation rate

Superscript

R = resolved

I. Introduction

AT SUPERSONIC speed, aerodynamic bodies with a blunt base such as missiles, rockets, and projectiles have recirculating flow in the base region. The associated low pressure causes base drag, which can constitute up to 35% of the total drag, as shown in flight tests with projectiles [1]. Small changes in the flow behavior may change the base pressure and therefore the performance of the entire flight vehicle. Numerous research efforts have focused on understanding the physics of the base flow and methods to alter or control the flow such that the base pressure would increase, which might be highly rewarding with respect to drag reduction and enhancing the performance characteristics of flight vehicles. By exploiting hydrodynamic instabilities in the flow, efficient modifications of the near wake can be achieved in the form of passive control such as base bleeding, boat tailing, base burning, etc., or active flow control.

Despite the simple geometry considered here, the base flow has a highly complex mean flowfield. A schematic of the mean flowfield is shown in Fig. 1. A supersonic freestream flow is aligned with a cylindrical body, producing an approach boundary layer (label 1 in Fig. 1) that separates at the base and undergoes an expansion (label 2) with a large turning angle, causing a strong reduction in pressure. A free shear layer (label 3) forms, separating the outer inviscid fluid from a large recirculation region (label 4) downstream of the base. As the free shear layer approaches the axis of symmetry, a recompression process (label 5) occurs that realigns the flow with

---

Presented as Paper 479 at the 44th AIAA Aerospace Sciences Meeting and Exhibit, Reno, NV, 9–12 January 2006; received 2 November 2006; revision received 24 April 2007; accepted for publication 1 May 2007.

[*] Research Assistant, Department of Aerospace and Mechanical Engineering. Member AIAA.

[†] Department of Aerospace and Mechanical Engineering; currently Lecturer, School of Engineering Sciences, University of Southampton, Southampton, SO17 1BJ England, United Kingdom. Member AIAA.

[‡] Department of Aerospace and Mechanical Engineering; currently Research Associate, Institute for Hydromechanics, University of Karlsruhe, 76128 Karlsruhe, Germany. Member AIAA.

[§] Professor, Department of Aerospace of Mechanical Engineering. Member AIAA.

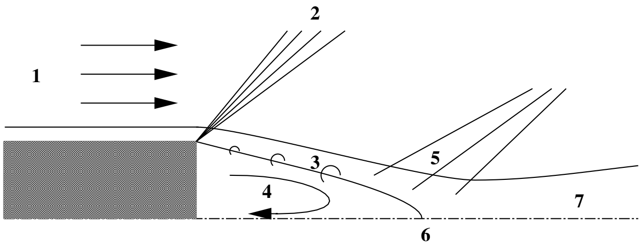

Fig. 1 Schematic of the physical problem.

the axis and subjects the shear layer to a strong adverse pressure gradient. The location at which the mean axial velocity at the axis is zero is defined as the reattachment point (label 6) that separates the region of reverse flow from the trailing wake (label 7).

Sandberg and Fasel [2–5] conducted direct simulations of supersonic base flows at a Mach number of 2.46 and Reynolds numbers between 30,000 and 100,000 to study the evolution of coherent structures and to investigate the hydrodynamic stability behavior of the near-wake region. Their work provided an insight into the instability mechanisms that lead to the formation of large coherent structures. These structures are deemed to be responsible for decreasing the base pressure and are thereby increasing the drag of axisymmetric aerodynamic bodies. The existence of such large coherent structures in supersonic base flows has been confirmed experimentally by Bourdon and Dutton [6,7]. It is therefore interesting to find out how the dynamics and strength of such structures are altered when flow control methods are applied. Of particular interest is to identify what distinguishes a successful from a less successful drag-reduction method with respect to the coherent structures.

Direct numerical simulation (DNS) of these flowfields at Reynolds numbers of $\mathcal{O}(10^6)$, as in the experiments at the University of Illinois at Urbana–Champaign, with a sufficient resolution in all three space dimensions and in time is out of reach even with present-day supercomputers. Alternative simulation approaches for computing such flows have to be considered, such as solving the Reynolds-averaged Navier–Stokes (RANS) equations or large eddy simulation (LES). RANS models can provide accurate mean flow results for many flows of practical interest. Unfortunately, RANS models often fail to provide accurate results for separated flows and are not suited for the present investigation, because they cannot provide any (reliable) information on coherent structures, even if operated in an unsteady fashion (URANS). LES, on the other hand, is able to capture these large-scale, three-dimensional, unsteady flow structures. Nevertheless, for high Reynolds numbers (in particular, near walls), LES can still be computationally too expensive to be feasible. As a cost-effective alternative, the idea of hybrid RANS/LES methods has emerged in the literature over the last several years. This technique aims to combine the advantages of LES and RANS into one model, such that LES is only performed when necessary and RANS is computed in the remainder of the computational domain. A variety of hybrid methods have been applied to investigate supersonic base flows by Forsythe et al. [8], Sandberg and Fasel [5,9], and Kawai and Fujii [10].

In the present study, to allow for an accurate prediction of the unsteady coherent structures, DNS is performed for supersonic base flows at $Re_D = 30,000$ with active and passive control of the wake. The resulting flow structures are studied and compared with the flow with no control. For base flows at $Re_D = 100,000$, due to the high-resolution requirements, we will rely on a hybrid methodology. The flow simulation methodology (FSM) is chosen, because it was already successfully employed for the identical flow configuration [5,9].

II. Simulation Methods

In direct numerical simulations, the three-dimensional unsteady Navier–Stokes equations are solved numerically without any further modeling assumptions. Therefore, all length and time scales need to be resolved by the computational grid. The flow simulation methodology is a strategy to provide the proper amount of modeling of the subgrid scales based on the local and instantaneous physical resolution of the calculation. This is accomplished by employing a so-called contribution function that locally and instantaneously compares the smallest relevant turbulent scales to the local computational grid size. The contribution function has to be designed such that it provides no modeling if the computation is locally well resolved so that the computation approaches a DNS in the fine-grid limit or such that it provides modeling of all scales in the coarse-grid limit and thus approaches a RANS calculation. Between these resolution limits, a well-designed contribution function adjusts the necessary modeling for the unresolved scales, and the larger (resolved) scales are computed as in traditional LES. However, in contrast to traditional LES, the subgrid scales are now modeled using a two-equation turbulence model. For the present investigation, a state-of-the-art explicit algebraic Reynolds stress model (EASM) is used. For a detailed discussion of FSM, see Fasel et al. [11,12].

A. Governing Equations

The conservation of mass, momentum, and total energy governs the physical problem under consideration. The fluid is assumed to be an ideal gas with constant specific heat coefficients. All quantities are made dimensionless using the flow quantities at a reference location in the flow; here, the freestream/inflow location is used. The radius of the body was chosen as the reference length. Applying a filter to the governing equations yields the nondimensional equations for the resolved flow quantities. The resolved continuity, momentum, and energy equations are

$$\frac{\partial \bar{\rho}}{\partial t} + \frac{\partial}{\partial x_k}(\bar{\rho}\tilde{u}_k) = 0 \tag{1}$$

$$\frac{\partial}{\partial t}(\bar{\rho}\tilde{u}_i) + \frac{\partial}{\partial x_k}[\bar{\rho}\tilde{u}_i\tilde{u}_k + \bar{p}\delta_{ik} - (\bar{\tau}_{ik} - \bar{\rho}\sigma_{ik})] = 0 \tag{2}$$

$$\frac{\partial}{\partial t}(\bar{\rho}E_R) + \frac{\partial}{\partial x_k}[\bar{\rho}\tilde{u}_k H + \bar{q}_k + Q_k - \tilde{u}_i(\bar{\tau}_{ik} - \bar{\rho}\sigma_{ik})] = \Pi \tag{3}$$

The resolved pressure is obtained from the equation of state:

$$\bar{p} = \frac{\bar{\rho}\tilde{T}}{\gamma M^2} \tag{4}$$

with $\gamma = 1.4$. The resolved heat flux is computed from

$$\bar{q}_k = -\frac{\kappa}{(\gamma - 1)M^2 Pr Re}\frac{\partial \tilde{T}}{\partial x_k} \tag{5}$$

with $Pr = 0.7$.

The preceding equations contain three terms that do not occur in the unfiltered equations: the subgrid stress tensor $\bar{\rho}\sigma_{ik}$, the subgrid heat-flux vector Q_k, and the source term Π in the energy equation; these terms have to be modeled. For a DNS, in which it is assumed that all relevant time and length scales are resolved by the computational grid and a sufficiently small time step, the model terms are set to zero, implying that $\phi = \bar{\phi} = \tilde{\phi}$. In the other limit, in which the filter width is so large that all fluctuations are filtered out, a traditional RANS is recovered.

For modeling the unresolved scales, turbulence models are employed that require the turbulent kinetic energy K and the turbulent dissipation rate ε. The additional variables are obtained by solving two transport equations:

$$\frac{\partial}{\partial t}(\bar{\rho}K) + \frac{\partial}{\partial x_k}\left[\bar{\rho}\tilde{u}_k K - \left(\frac{\bar{\mu}}{Re} + \frac{\mu_T}{\sigma_K}\right)\frac{\partial K}{\partial x_k}\right] = \Pi_K \tag{6}$$

$$\frac{\partial}{\partial t}(\bar{\rho}\varepsilon) + \frac{\partial}{\partial x_k}\left[\bar{\rho}\tilde{u}_k \varepsilon - \left(\frac{\bar{\mu}}{Re} + \frac{\mu_T}{\sigma_\varepsilon}\right)\frac{\partial \varepsilon}{\partial x_k}\right] = \Pi_\varepsilon \tag{7}$$

The turbulent viscosity μ_T is given as

$$\mu_T = c_\mu \tau_T K \tag{8}$$

with $c_\mu = 0.09$. Additional constants for the turbulent diffusion terms are $\sigma_K = 1.0$ and $\sigma_\varepsilon = 1.3$.

1. *Source Terms*

The source terms Π and Π_K in the energy and K equations include a pressure-dilatation term, terms involving the turbulent dissipation rate, and the subgrid mass flux. It was shown by Sarkar et al. [13] that both pressure dilatation and compressible dissipation are important in compressible turbulence. Therefore, both effects are modeled according to Sarkar et al. [13], Sarkar [14], and Speziale [15]:

$$\begin{aligned}\Pi = {} & (1 - a_2 M_T)\bar{\rho}\sigma_{ik}\tilde{S}_{ik} + \left(1 - a_3 M_T^2\right)\bar{\rho}\varepsilon \\ & + (\bar{\tau}_{ik} - \bar{p}\delta_{ik})\frac{\partial}{\partial x_k}\left[\frac{\mu_T}{\sigma_\rho}\frac{\partial}{\partial x_i}\left(\frac{1}{\bar{\rho}}\right)\right]\end{aligned} \tag{9}$$

$$\begin{aligned}\Pi_K = {} & -(1 - a_2 M_T)\bar{\rho}\sigma_{ik}\tilde{S}_{ik} - \left(1 - a_3 M_T^2\right)\bar{\rho}\varepsilon \\ & - \left(\frac{\partial p}{\partial x_i} - \frac{\partial \tau_{ik}}{\partial x_k}\right)\frac{C_\mu}{\bar{\rho}\sigma_\rho}\tau K \frac{\partial \bar{\rho}}{\partial x_i}\end{aligned} \tag{10}$$

with the constants $\sigma_\rho = 0.5$, $a_2 = 0.15$, and $a_3 = 0.2$.

$$\begin{aligned}\Pi_\varepsilon = {} & -C_{\varepsilon 1}\bar{\rho}\frac{1}{\tau_T}\sigma_{ik}\left(\frac{\partial \tilde{u}_i}{\partial x_k} - \frac{1}{3}\tilde{S}_{jj}\delta_{ik}\right) - C_{\varepsilon 2} f_{\varepsilon_2}\bar{\rho}\frac{\varepsilon}{\tau_T} \\ & + C_{\varepsilon 3}\bar{\rho} Re_T^{\frac{1}{2}}\frac{\varepsilon}{\tau_T} - \frac{4}{3}\bar{\rho}\varepsilon\tilde{S}_{jj}\end{aligned} \tag{11}$$

where $f_{\varepsilon 2}$ is a wall-damping function, $C_{\varepsilon 1} = 1.44$, $C_{\varepsilon 2} = 1.83$, $C_{\varepsilon 3} = 0.001$, and Re_T is the turbulent Reynolds number:

$$Re_T = \frac{\bar{\rho} K}{\bar{\mu}}\tau_T \tag{12}$$

To remove singularities at walls in the destruction term of the ε equation (i.e., $K = 0$), a damping function $f_{\varepsilon 2}$ is used. Traditionally, this wall-damping function takes the form

$$f_{\varepsilon 2}(N) = 1 - \exp(-Re\sqrt{0.1K}N) \tag{13}$$

where N is the wall-normal distance. In the EASM model implemented here (described next), this wall-damping function is the only term containing the wall distance; the Reynolds stress model automatically accounts for near-wall effects through the computation of α_1/τ. To be completely independent of the wall distance, another approach is used for computing $f_{\varepsilon 2}$ that is based on a suggestion by Durbin [16]. It relies on the assumption that the smallest physical time scale in a turbulent flow is the Kolmogorov time scale. Therefore, by computing $f_{\varepsilon 2}$ as

$$f_{\varepsilon 2} = \frac{1}{\max[1, \frac{C_T}{\sqrt{Re_T}}]} \tag{14}$$

a completely wall-distance-independent model is obtained. This function contains an additional constant that was calibrated in Sandberg [17].

2. *Reynolds Stress Model*

As mentioned earlier, the flow under investigation features physically very disparate regions such as a boundary layer, a free shear layer subject to pressure gradients, and a recirculation region. It is safe to say that assuming the production-to-dissipation ratio to be a constant cannot hold for all regions; for this reason, the EASM as presented in Rumsey et al. [18] was chosen. In this model, the production-to-dissipation ratio is *not* fixed to a constant, but computed locally and instantaneously. To locally determine the ratio of turbulent production-to-dissipation rate, the roots of a cubic equation have to be solved. The turbulent stress tensor is computed from

$$\begin{aligned}\bar{\rho}\sigma_{ik}^R = {} & \frac{2}{3}\bar{\rho}K\delta_{ik} - 2\mu_T\Bigg[\left(\tilde{S}_{ik} - \frac{1}{3}S_{jj}\delta_{ik}\right) \\ & + a_2 a_4(\tilde{S}_{ij}\tilde{W}_{ik} + \tilde{S}_{kj}\tilde{W}_{ji}) - 2a_3 a_4\left(\tilde{S}_{ij}\tilde{S}_{jk} - \frac{1}{3}\tilde{S}_{lm}\tilde{S}_{lm}\delta_{ik}\right)\Bigg]\end{aligned} \tag{15}$$

The turbulent viscosity for the EASM is given by

$$\mu_T = -\bar{\rho}K\tau_T\left(\frac{\alpha_1}{\tau_T}\right) \tag{16}$$

Note that the turbulent viscosity used by the EASM is not the same as that used for the turbulent heat-flux vector and the transport equations for K and ε.

The value of α_1/τ_T is obtained by locally and instantaneously solving the following cubic equation:

$$\left(\frac{\alpha_1}{\tau_T}\right)^3 + p\left(\frac{\alpha_1}{\tau_T}\right)^2 + q\left(\frac{\alpha_1}{\tau_T}\right) + r = 0 \tag{17}$$

where

$$p = -\frac{\gamma_1}{\phi\gamma_0}$$

$$q = \frac{1}{(2\phi\gamma_0)^2}\left(\gamma_1^2 - 2\phi\gamma_0 a_1 - \frac{2}{3}\phi a_3^2 - 2W^2\tau_T^2 a_2^2\right)$$

$$r = \frac{\gamma_1 a_1}{(2\phi\gamma_0)^2}$$

The needed parameters are assembled as follows:

$$\phi = \tilde{S}_{ik}\tilde{S}_{ik}\tau_T^2, \qquad W = -\tilde{W}_{ik}\tilde{W}_{ik}, \qquad a_4 = \frac{\tau_T}{\gamma_1 - 2\gamma_0(\frac{\alpha_1}{\tau_T})\phi}$$

$$\gamma_0 = \frac{C_1^1}{2}, \qquad \gamma_1 = \frac{C_1^0}{2} + \left(\frac{C_{\epsilon 2} - C_{\epsilon 1}}{C_{\epsilon 1} - 1}\right)$$

The constants are given as $C_{\epsilon 1} = 1.44$, $C_{\epsilon 2} = 1.83$, $C_1^0 = 3.4$, $C_1^1 = 1.8$, $a_1 = 0.4866$, $a_2 = 0.8$, and $a_3 = 0.375$.

For the flow simulation methodology, the turbulent stress tensor is multiplied with the contribution function $f(\Delta/L)$:

$$\sigma_{ik} = f(\Delta/L)\sigma_{ik}^R \tag{18}$$

For the compressible extension [12,19], the source term in the energy equation and the turbulent heat-flux vector have to be rescaled with the same contribution function:

$$Q_k = f(\Delta/L)Q_k^R \quad \text{and} \quad \Pi = f(\Delta/L)\Pi^R \tag{19}$$

The term $\Delta = [(\Delta z^2 + \Delta r^2 + (r\Delta\theta)^2)/3]^{1/2}$ is the representative computational grid size, and L is the relevant length scale. In the present calculations, a contribution function in a form proposed by Speziale [19] was used:

$$f(\Delta/L_k) = (1 - e^{-\beta\frac{\Delta}{L_k}})^n \tag{20}$$

where L_k is the Kolmogorov length scale $L_k = (\mu/\rho Re)^{3/4}/\epsilon^{1/4}$, and β and n are adjustable parameters. Following Speziale [19], n is set to unity and β is set to a small value of $\mathcal{O}(10^{-3})$. Other forms of the contribution function and different choices of the length scale are possible [11].

As the ratio $\beta\Delta/L_k$ becomes small (grid resolution sufficient to resolve the relevant scales), $f(\Delta/L_k)$ approaches zero and the computation will approach the DNS limit. For insufficient resolution, $f(\Delta/L_k)$ approaches unity and the RANS limit is approached. For all intermediate values of the contribution function, a LES based on a state-of-the-art Reynolds stress model is performed.

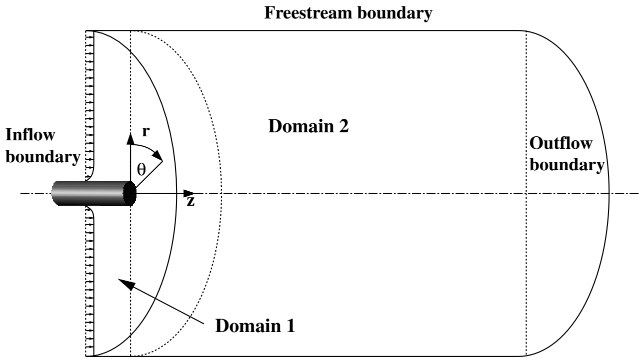

Fig. 2 Computational domain.

B. Numerical Method

For DNS, the compressible Navier–Stokes equations in cylindrical coordinates are solved using sixth-order-accurate split compact differences in the radial direction, fourth-order-accurate split differences in the streamwise direction, and a pseudospectral discretization in the azimuthal direction. To preserve accuracy, the finite differences are derived for nonequidistant grids. A state-of-the-art axis treatment is implemented, exploiting parity conditions [20]. For the time advancement, a standard fourth-order Runge–Kutta scheme is employed. The computational domain is shown in Fig. 2.

For FSM calculations, the fully three-dimensional turbulent transport equations, including all compressible extensions, are solved with the same time and space discretization as that used for the DNS code. Therefore, the Reynolds stresses are also computed with a high-order-accurate scheme. Only the density gradients are computed with second-order-accurate difference approximations to allow for some numerical dissipation in which shocks and expansion waves are present in the flow. Note that the calibration constant β in the contribution function of FSM is set to $\beta = 4 \times 10^{-3}$ for the present investigation, following previous base flow simulations [5].

C. Flow Control Methods

Vortex generators are one of the passive means to modify the near-wake characteristics of base flows and, hence, the base pressure. In the present investigation, this is accomplished by introducing steady disturbances into the approach boundary layer, just upstream of separation (center of disturbance at $r = 1.05$ and $z = -0.15$) by a steady volume force $\hat{F}^k_{\mathrm{VF}}$. The volume force was added to the right-hand side (RHS) of the radial momentum equation in Fourier space, thus a specific azimuthal mode could be forced. The disturbances can be either steady for passive flow control or periodic in time for active flow control, with a frequency ω and a disturbance amplitude A_{dist}:

$$\hat{F}^k_{\mathrm{VF}} = A_{\mathrm{dist}} \sin(2\pi\omega t)\left[1 - \cos\left(\frac{(r - r_b)\pi}{r_e - r_b}\right)\right] \times \left[1 - \cos\left(\frac{(z - z_b)\pi}{z_e - z_b}\right)\right] \tag{21}$$

with k denoting which azimuthal mode is forced and r_b, r_e, z_b, and z_e being the starting and end points of the forcing in the radial and the streamwise directions, respectively.

Two separate forcing mechanisms (steady or unsteady) for altering the near wake were investigated:

1) By emulating vortex generators using steady disturbances, longitudinal vortices were introduced into the initial shear layer, imposing symmetries on the flow in the r–θ plane and constraining helical modes with low mode numbers.

2) Axisymmetric periodic perturbations were introduced that, due to compressibility effects, do not experience significant amplification in the streamwise direction, but should reduce the energy transfer from the mean flow to oblique disturbances, thereby decreasing the growth of helical instability modes.

III. Results and Discussion

A. DNS for $Re_D = 30,000$

Hydrodynamic stability investigations performed by Sandberg and Fasel [2–4], using both spatial and temporal simulations, concluded that the azimuthal modes $k = 1$, 2, 3, and 4 are the dominant modes for supersonic axisymmetric wakes at $Re_D = 30,000$. In particular, mode $k = 2$ is responsible for a "four-lobe" wake structure of the mean flow and significant entrainment of fluid from the recirculation region and, consequently, a low base pressure.

The knowledge gained from these calculations motivated the use of flow control methods to exploit and/or counteract the instability mechanisms present in the flow, such that a base-pressure increase and, consequently, a drag reduction could be accomplished. Toward that end, several DNS calculations were conducted at $M = 2.46$ and $Re_D = 30,000$ employing flow control, such that the dominance of the low-wave-number modes would be weakened. For this study, the same computational grid as that reported in Sandberg and Fasel [4] was chosen.

To emulate passive flow control using steady vortex generators that introduce longitudinal vorticity into the shear layer, the volume force $\hat{F}^k_{\mathrm{VF}}$ was added to a specific azimuthal mode of the RHS with $\omega = 0$. Three cases were examined: forcing either mode $k = 4$, 8, or 16, hence generating 8, 16, or 32 counter-rotating longitudinal structures in the circumferential direction. The resulting structures are illustrated in Fig. 3 by contours of streamwise vorticity in end views at a location close to the base ($z = 1$). For active flow control, the axisymmetric mode $k = 0$ was disturbed periodically with $\omega = 0.4166$. This frequency was selected because it corresponds to the most unstable streamwise wavelength for the axisymmetric mode that was found from previous stability investigations [17].

To determine how the different forcing mechanisms affect the generation and evolution of coherent structures, visualizations of instantaneous isocontours of $Q = 0.1$ are shown in Fig. 4. For the case employing periodic axisymmetric forcing (Fig. 4b), the vortices appearing in the trailing wake are very similar to the unforced case. The axisymmetric structures generated just upstream of separation by the periodic forcing can be observed in the shear layer. However, an azimuthal modulation caused by the dominant helical modes is visible. Also, when employing steady forcing of mode $k = 4$, the

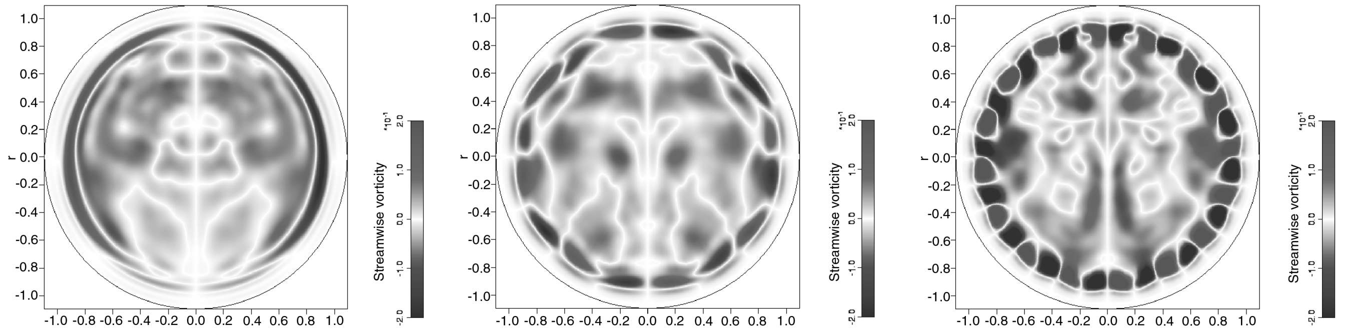

Fig. 3 End views of time-averaged streamwise vorticity in the initial shear layer at $z = 1$; steady azimuthal forcing of $k = 4$, $k = 8$, and $k = 16$ from left to right; DNS for $Re_D = 30,000$.

a) Unforced b) Periodic axisymmetric forcing c) Steady forcing of $k = 4$

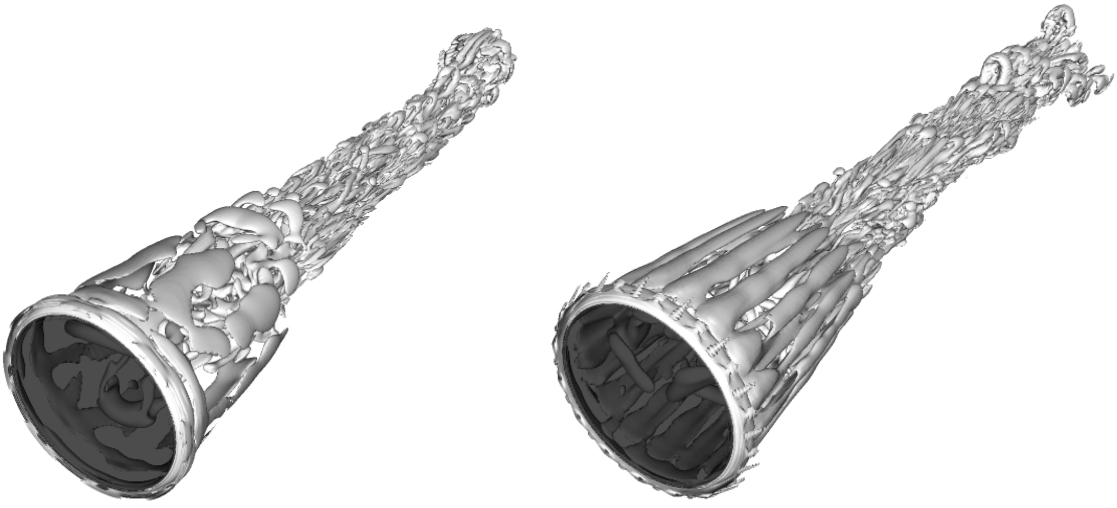

d) Steady forcing of $k = 8$ e) Steady forcing of $k = 16$

Fig. 4 Perspective view from inflow toward outflow of instantaneous isocontours of $Q = 0.1$ for unforced and forced cases; DNS for $Re_D = 30,000$; the dark shaded area represents the base of the body.

resulting base flow appears to be very similar to the unforced case. This confirms that $k = 4$ is a significant mode in the natural unforced case. When mode $k = 8$ is forced instead, longitudinal vortices emerge from the forcing location and can be observed in the initial shear layer. Also, a considerably larger number of longitudinal structures can be observed than for the unforced case or the two forced cases discussed earlier. The diameter of these streamwise vortices appears to be smaller than for the other cases as well. Using steady forcing of mode $k = 16$ (Fig. 4e), longitudinal structures, originating in the approach flow, can be observed in the shear layer. As for the case in which $k = 8$ is forced, a denser clustering of streamwise structures with a reduced diameter (versus the unforced case) can be detected in the recompression region and in the trailing wake. In the unforced case, the streamwise vortices within the recirculation region are most likely a consequence of secondary/tertiary instabilities that occur when low-wave-number unstable modes are present [3,17]. For the forced cases, the introduced longitudinal structures cause a strong azimuthal variation of the shear layer, thereby leading to the formation of an even greater number of streamwise structures than in the unforced case.

A flapping motion of the far wake, as for the unforced case, can be observed for most forced cases, implying that the contribution of mode $k = 1$ is considerable in this region. However, for the cases in which steady forcing is applied with modes $k = 8$ or $k = 16$, no significant lateral movement was observed for the near wake or the initial trailing wake, suggesting that the introduction of longitudinal vortices can prevent low-wave-number modes from becoming dominant in this region.

The time-averaged streamwise velocity along the axis and the mean pressure coefficient along the base from the forced cases are compared with the unforced case in Fig. 5. Periodic forcing of the axisymmetric mode results in a streamwise axis-velocity distribution similar to that obtained from the unforced case. However, the mean pressure coefficient at the base is increased by approximately 3.5%. On the other hand, for steady forcing of higher azimuthal modes ($k = 4$ or $k = 8$), the recirculation length is slightly decreased. When forcing $k = 16$, an even further reduction of the recirculation length can be observed. Responsible for this reduction is the increased mixing caused by the larger number of longitudinal structures in the shear layer. It is noteworthy, however, that in the near-wake region, the curves of the streamwise axis velocity versus downstream distance differ significantly for the cases with forcing at higher modes. When forcing mode $k = 4$, the data closely follow that of the unforced case. In contrast, when mode $k = 8$ is forced, the slope at the base becomes shallower, but the profile dips to the same value of reverse velocity obtained from all other cases farther downstream. For the case, in which the largest number of streamwise vortices is introduced into the shear layer, the opposite is the case and the slope at the base becomes steeper. The changing behavior of the streamwise axis-velocity distribution also translates to different mean pressure values at the base. When forcing mode $k = 4$, a pressure distribution on the base is obtained that is very similar to the case in which axisymmetric periodic forcing was employed. Forcing mode $k = 8$ appears to be the most successful in augmenting base pressure, showing a 4.5% increase compared with the unforced case. For the case in which $k = 16$ is forced, the gain in preventing the dominance of the low wave numbers seems to be outweighed by the increased mixing in the shear layer, leading to a slightly decreased pressure coefficient on the base.

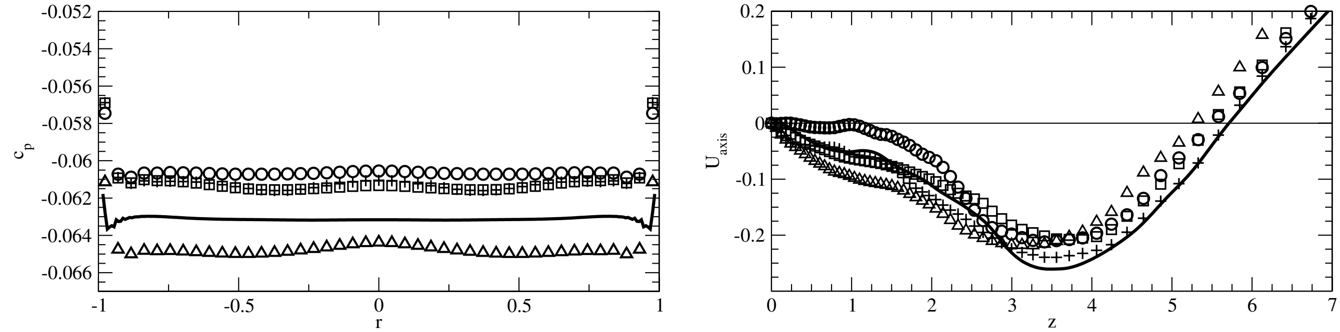

Fig. 5 Pressure coefficient on the base (left) and streamwise velocity along the axis of symmetry (right); unforced case (solid line), periodic forcing of $k = 0$ with $\omega = 0.4166$ (+), steady forcing of $k = 4$ (□), steady forcing of $k = 8$ (○), steady forcing of $k = 16$ (△); DNS for $Re_D = 30,000$.

B. FSM for $Re_D = 100,000$

FSM was validated against DNS and experimental data and was employed to investigate transitional and turbulent supersonic base flows at $M = 2.46$ and $Re_D = 30,000$ to 3.3×10^6 by Sandberg and Fasel [5,9]. Here, for the transitional supersonic base flow at $M = 2.46$ and $Re_D = 100,000$, FSM with the same computational setup is employed to assess the effect of Reynolds number on the efficiency of the flow control mechanisms investigated for $Re_D = 30,000$ using DNS (see the preceding discussion). Note that because the flow is transitional, a fine resolution is required in the initial shear layer to resolve the dominant instability waves. As a consequence, FSM attempts for an almost DNS-like solution very close to the base, and the role of the turbulence modeling is to allow for coarser grids farther downstream, once large coherent structures have already been formed. Nevertheless, the value of the contribution function did not exceed 0.1 or 10% in the whole computational domain; that is, FSM operated as a (nontraditional) LES. As such, the choice of the form of the contribution function as proposed by Speziale [19] [see Eq. (20)] that compares the grid size to a length scale representing the dissipative scales seems appropriate, because it essentially determines how much of the dissipation needs to be provided by the turbulence model.

For reference and comparison, in Fig. 6, dominant flow structures are shown for the unforced wake. Shown are perspective top and side views of isocontours of $Q = 0.05$ obtained from an FSM calculation of the unforced case at $Re_D = 100,000$. Helical structures can be observed in the shear layer close to the base. In addition, a large number of longitudinal structures can be seen within the recirculation region, and hairpin vortices are present downstream of the recompression region.

For $Re_D = 100,000$, FSM calculations were performed with steady forcing of modes $k = 2$, 4, 8, and 16 and periodic forcing of the zeroth mode $k = 0$. Contours of time-averaged streamwise vorticity of end views at $z = 1$ are shown in Fig. 7 to illustrate the different development of the structures in the shear layer when employing steady forcing. Visualizations of instantaneous isocontours of $Q = 0.05$ are shown in Fig. 8. When steady forcing with an amplitude $A_{\text{dist}} = 1.0$ is applied to the azimuthal/helical modes $k = 2$ and 4 (see Figs. 8a and 8b), the flowfield resembles the unforced case and no significant longitudinal vortices emerging from the forcing location can be observed. However, once the higher modes $k = 8$ and 16 are forced (see Figs. 8c and 8d), the flowfield differs considerably from the unforced case. As in the lower Reynolds number case investigated using DNS, longitudinal structures can be seen emanating from the forcing location, with the azimuthal spacing of these structures decreasing for the higher mode numbers. Overall, when steady forcing of the higher modes is employed, energetic longitudinal structures are produced that increase the mixing within the recirculation region.

When applying periodic axisymmetric forcing, several different frequencies were investigated. First, calculations were carried out with a frequency $\omega = 0.4166$, which corresponds to the most unstable frequency of the axisymmetric mode at $Re_D = 30,000$. However, for the unforced case at $Re_D = 100,000$, DNS conducted by Sandberg and Fasel [2–4] revealed that a significant amount of energy is contained in frequencies with a Strouhal number greater

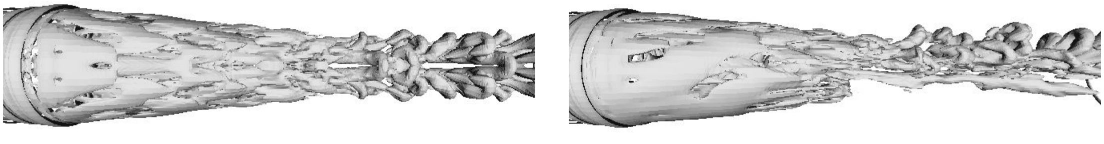

a) Top view

b) Side view

Fig. 6 Instantaneous isocontours of $Q = 0.05$ for the unforced case with flow from left to right; FSM for $Re_D = 100,000$.

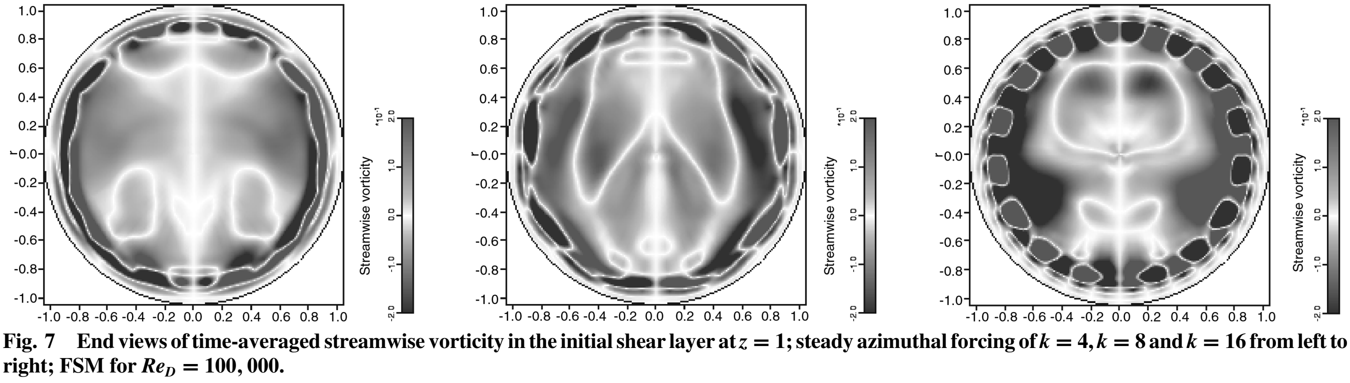

Fig. 7 End views of time-averaged streamwise vorticity in the initial shear layer at $z = 1$; steady azimuthal forcing of $k = 4$, $k = 8$ and $k = 16$ from left to right; FSM for $Re_D = 100,000$.

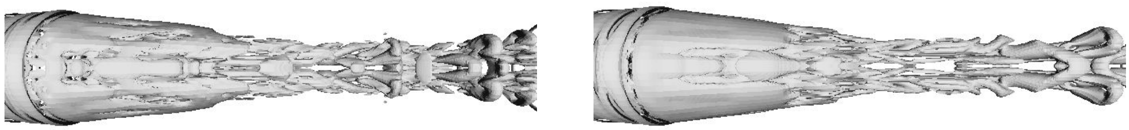

a) Steady forcing of $k = 2$ b) Steady forcing of $k = 4$

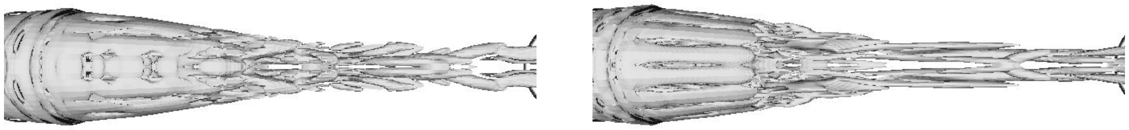

c) Steady forcing of $k = 8$ d) Steady forcing of $k = 16$

Fig. 8 Perspective top view with flow from left to right of instantaneous isocontours of $Q = 0.05$ for steady-forcing cases with $A_{\text{dist}} = 1.0$; FSM for $Re_D = 100,000$.

a) $\omega = 0.4166$ b) $\omega = 1.0$

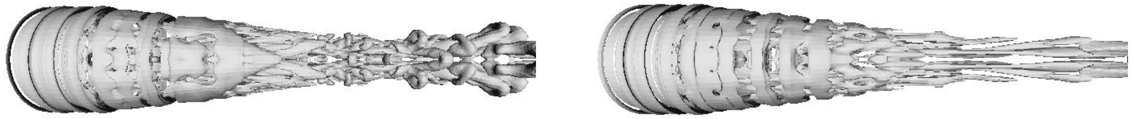

c) $\omega = 2.0$ d) $\omega = 2.5$

Fig. 9 Perspective top view with flow from left to right of instantaneous isocontours of $Q = 0.05$ for periodic forcing cases with $A_{\text{dist}} = 1.0$; FSM for $Re_D = 100,000$.

than one. This suggests that a strong response might occur when forcing at higher frequencies. Therefore, a range of higher frequencies ($\omega = 1.0$, 2.0, and 2.5) was investigated. Results from these investigations are shown in Fig. 9. Axisymmetric structures generated just upstream of the corner separation can be observed in the shear layer. However, the azimuthal modulation due to the dominant helical modes is less pronounced than was observed at $Re_D = 30,000$. When the axisymmetric mode was forced with amplitude $A_{\text{dist}} = 1.0$ and frequency $\omega = 0.4166$, the flow structures far downstream from the base resemble those of the unforced flow. Higher frequencies ($\omega = 1.0$ and 2.0) produce an increasing number of axisymmetric structures, but far downstream the flow is still similar to the unforced flowfield. Finally, when a high frequency ($\omega = 2.5$) is used, the hairpin vortices that are present in the trailing wake for the unforced flow and low-frequency cases disappear. It is suggested that at this high frequency, the energy otherwise transferred to the helical structures is now transferred to the axisymmetric mode, which does not exhibit significant spatial growth. Because the helical modes are far less energetic in this case, the formation of hairpin vortices is suppressed.

The time-averaged pressure coefficient along the base and the streamwise velocity along the axis are shown in Fig. 10 for steady forcing of the higher azimuthal modes and for the unforced reference case. When forcing mode $k = 2$, the recirculation length is slightly increased, resulting in a slight pressure increase. When forcing azimuthal modes with $k > 2$, the recirculation length decreases due to the entrainment of low-speed fluid from the recirculation region, as seen already in the earlier investigation of base flows at $Re_D = 30,000$. However, in contrast to the lower Reynolds number cases, the base pressure also decreases for all calculations in which steady forcing was applied to $k > 2$. This is in agreement with experiments at an even higher Reynolds number by Bourdon and Dutton [7], who did not find an increase in base pressure when generating longitudinal vortices by means of tabs on the axisymmetric body.

For periodic forcing of the axisymmetric mode, the time-averaged base-pressure coefficient and the streamwise axis velocity are shown in Fig. 11. When forcing with a frequency $\omega = 0.4166$, the recirculation length is decreased and, in contrast to the lower Reynolds number case, the base pressure is considerably decreased. But as the frequency increases, both the recirculation length and the base pressure increase. In fact, for $\omega = 2.5$, the base pressure is increased by 5% over the unforced case. This result is consistent with the findings of Bourdon and Dutton [7], who found an increase in base pressure only when forcing the axisymmetric mode. Note, however, that in the experiment, mode $k = 0$ was forced using an

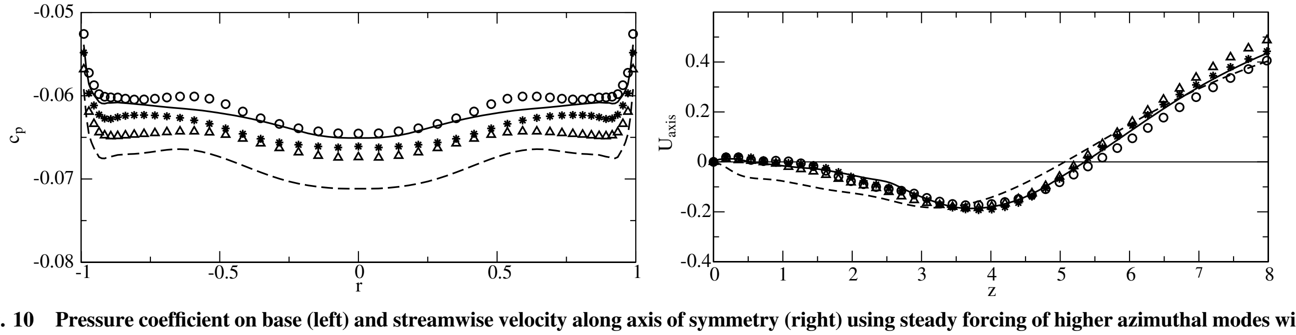

Fig. 10 Pressure coefficient on base (left) and streamwise velocity along axis of symmetry (right) using steady forcing of higher azimuthal modes with $A_{\text{dist}} = 1.0$; unforced case (solid line), forcing $k = 2$ (○), forcing $k = 4$ (△), forcing $k = 8$ (*), forcing $k = 16$ (dashed line); FSM for $Re_D = 100,000$.

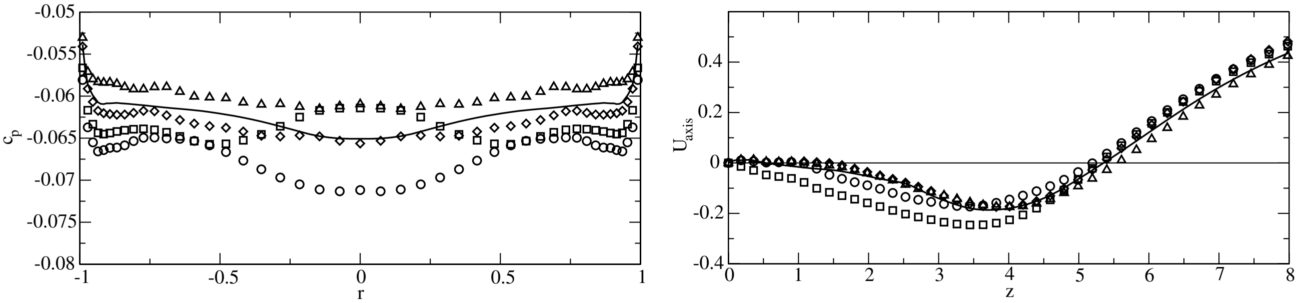

Fig. 11 Pressure coefficient on base (left) and streamwise velocity along axis of symmetry (right) for cases with periodic forcing of axisymmetric mode; $k = 0$ and $A_{\mathrm{dist}} = 1.0$; unforced case (solid line), $\omega = 0.4166$ (○), $\omega = 1.0$ (□), $\omega = 2.0$ (◇), $\omega = 2.5$ (△); FSM for $Re_D = 100,000$.

axisymmetric trip (i.e., with a steady perturbation), in contrast to the periodic forcing in our simulations.

IV. Conclusions

DNS calculations were conducted for transitional supersonic base flows at $M = 2.46$ and $Re_D = 30,000$. Active and passive flow control techniques were applied and it was demonstrated that the base pressure can be increased. Forcing the axisymmetric mode had the same effect as that observed in experiments [7] for a much higher Reynolds number and a fully turbulent approach flow. When applying steady forcing of higher azimuthal modes, longitudinal structures emerge from the forcing location, leading to a reduced flapping of the initial shear layer and a larger number of streamwise structures in the trailing wake. The longitudinal vortices introduced into the shear layer result in increased entrainment and a decreased recirculation length. Forcing modes $k = 4$ and $k = 8$ leads to an increase in base pressure, suggesting that preventing the dominance of the low-wave-number modes outweighs the increased mixing. This is in contrast to the observations made in higher Reynolds number experiments [7], in which the introduced longitudinal structures always reduced the base pressure.

For base flows at $Re_D = 100,000$, FSM calculations have been employed to investigate flow control. For $Re_D = 100,000$, consistent with high Reynolds number experiments [7], applying steady forcing of higher azimuthal modes and thereby generating longitudinal vortices in the shear layer does not succeed in reducing the base drag. In contrast, when forcing the axisymmetric mode, an increase of base pressure can be achieved. In the present study, it was shown that the degree of drag reduction varies with the frequency of the forcing, showing better results for increasing frequencies. Overall, from the present investigations, it is concluded that periodic forcing of the axisymmetric mode has the greatest potential with regard to drag reduction.

Acknowledgments

This work was supported by the U.S. Army Research Office (ARO) under grant number DAAD 19-02-1-0361 no. 1, with Thomas L. Doligalski serving as program manager. Computer time from the U.S. Department of Defense High-Performance Computing Modernization Program at the Engineer Research and Development Center (ERDC) and Major Shared Resource Center (MSRC) under Challenge project VI9ARONC11312C1D is also gratefully acknowledged.

References

[1] Rollstin, L., "Measurement of Inflight Base-Pressure on an Artillery-Fired Projectile," *Journal of Spacecraft and Rockets*, Vol. 27, No. 1, 1990, pp. 5–6.

[2] Sandberg, R. D., and Fasel, H. F., "Instability Mechanisms in Supersonic Base Flows," AIAA Paper 2004-0593, Jan. 2004.

[3] Sandberg, R. D., and Fasel, H. F., "Numerical Investigation of Transitional Supersonic Axisymmetric Wakes," *Journal of Fluid Mechanics*, Vol. 563, Sept. 2006, pp. 1–41.

[4] Sandberg, R. D., and Fasel, H. F., "Direct Numerical Simulations of Transitional Supersonic Base Flows," *AIAA Journal*, Vol. 44, No. 4, 2006, pp. 848–858.

[5] Sandberg, R. D. and Fasel, H. F., "Investigation of Supersonic Wakes Using Conventional and Hybrid Turbulence Models," *AIAA Journal*, Vol. 44, No. 9, 2006, pp. 2071–2083.

[6] Bourdon, C. J., and Dutton, J. C., "Planar Visualizations of Large Scale Turbulent Structures in Axisymmetric Supersonic Separated Flows," *Physics of Fluids*, Vol. 11, No. 1, 1999, pp. 201–213.

[7] Bourdon, C. J., and Dutton, J. C., "Visualizations and Measurements of Axisymmetric Base Flows Altered by Surface Disturbances," AIAA Paper 2001-0286, Jan. 2001.

[8] Forsythe, J. R., Hoffmann, K. A., Cummings, R. M., and Squires, K. D., "Detached-Eddy Simulation with Compressibility Corrections Applied to a Supersonic Axisymmetric Base Flow," *Journal of Fluids Engineering*, Vol. 124, No. 4, 2002, pp. 911–923.

[9] Sandberg, R. D., and Fasel, H., "Application of a New Flow Simulation Methodology for Supersonic Axisymmetric Wakes," AIAA Paper 2004-0067, Jan. 2004.

[10] Kawai, S., and Fujii, K., "Computational Study of Supersonic Base Flow Using Hybrid Turbulent Methodology," *AIAA Journal*, Vol. 43, No. 6, June 2005, pp. 1265–1275.

[11] Fasel, H. F., Seidel, J. J., and Wernz, S. H., "A Methodology for Simulation of complex Turbulent Flows," *Journal of Fluids Engineering*, Vol. 124, No. 4, 2002, pp. 933–942.

[12] Fasel, H. F., Von Terzi, D. A., and Sandberg, R. D., "A Methodology for Simulating Compressible Turbulent Flows," *Journal of Applied Mechanics*, Vol. 73, No. 3, May 2006, pp. 405–412.

[13] Sarkar, S., Erlebacher, G., Hussaini, M. Y., and Kreiss, H. O., "The Analysis and Modelling of Dilatational Terms in Compressible Turbulence," *Journal of Fluid Mechanics*, Vol. 227, June 1991, pp. 473–493.

[14] Sarkar, S., "The Pressure-Dilatation Correlation in Compressible Flows," *Physics of Fluids A*, Vol. 4, No. 12, Dec. 1992, pp. 2674–2682.

[15] Speziale, C. G., "Modeling of Turbulent Transport Equations," *Simulation and Modeling of Turbulent Shear Flows*, Oxford Univ. Press, New York, 1996.

[16] Durbin, P. A., "A Reynolds Stress Model for Near Wall Turbulence," *Journal of Fluid Mechanics*, Vol. 249, Apr. 1993, pp. 465–498.

[17] Sandberg, R. D., "Numerical Investigation of Transitional and Turbulent Supersonic Axisymmetric Wakes," Ph.D. Thesis, Department of Aerospace and Mechanical Engineering, Univ. of Arizona, Tucson, AZ, Dec. 2004.

[18] Rumsey, C. L., Gatski, T. B., and Morrison, J. H., "Turbulence Model Predictions of Strongly Curved Flow in a U-Duct," *AIAA Journal*, Vol. 38, No. 8, Aug. 2000, pp. 1394–1402.

[19] Speziale, C. G., "A Combined Large-Eddy Simulation and Time-Dependent RANS Capability for High-Speed Compressible Flows," *Journal of Scientific Computing*, Vol. 13, No. 3, Sept. 1998, pp. 253–74.

[20] Lewis, H. R., and Bellan, P. M., "Physical Constraints on the Coefficients of Fourier Expansions in Cylindrical Coordinates," *Journal of Mathematical Physics*, Vol. 31, No. 11, 1990, pp. 2592–2596.

R. Cummings
Associate Editor